ACS NANO
www.acsnano.org

ARTICLE

# Piezo-Phototronic Effect in a Quantum Well Structure

Xin Huang,[†,⊥] Chunhua Du,[†,⊥] Yongli Zhou,[†] Chunyan Jiang,[†] Xiong Pu,[†] Wei Liu,[†] Weiguo Hu,[*,†] Hong Chen,[*,§] and Zhong Lin Wang[*,†,‡]

[†]Beijing Institute of Nanoenergy and Nanosystems, Chinese Academy of Sciences, Beijing 100083, People's Republic of China
[‡]School of Materials Science and Engineering, Georgia Institute of Technology, Atlanta, Georgia 30332-0245, United States
[§]Beijing National Laboratory for Condensed Matter Physics, Institute of Physics, Chinese Academy of Sciences, Beijing 100190, People's Republic of China

Supporting Information

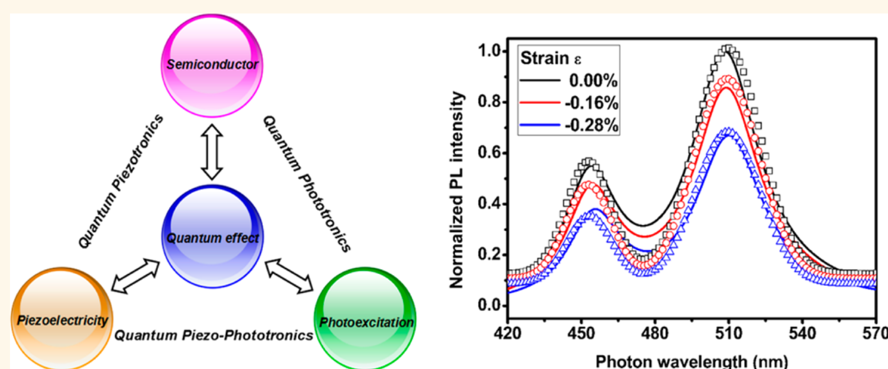


**ABSTRACT:** **With enhancements in the performance of optoelectronic devices, the field of piezo-phototronics has attracted much attention, and several theoretical works have been reported based on semiclassical models. At present, the feature size of optoelectronic devices are rapidly shrinking toward several tens of nanometers, which results in the quantum confinement effect. Starting from the basic piezoelectricity equation, Schrödinger equation, Poisson equation, and Fermi's golden rule, a self-consistent theoretical model is proposed to study the piezo-phototronic effect in the framework of perturbation theory in quantum mechanics. The validity and universality of this model are well-proven with photoluminescence measurements in a single GaN/InGaN quantum well and multiple GaN/InGaN quantum wells. This study provides important insight into the working principle of nanoscale piezo-phototronic devices as well as guidance for the future device design.**

**KEYWORDS:** *piezo-phototronic, quantum effect, perturbation theory, self-consistent calculation, photoluminescence measurements*

The piezo-phototronic effect, known as a three-way coupling of piezoelectric polarization,[1,2] semiconductor properties, and optical excitation,[3] has been demonstrated to improve the function and performance of optoelectronic devices, such as improvement of light emission efficiency in light-emitting diodes (LEDs),[4] responsivity enhancement of photodetectors,[5] efficiency optimization of optical fiber-based solar cells,[6] and a self-powered pressure–sensor matrix.[7] Behind the fundamental physics of the piezo-phototronic effect, several theoretical analyses and numerical simulations have been performed, including one-dimensional analytical modeling in p–n junction-based lighting diodes[8] and two-dimensional simulation considering device geometry,[9] to provide reasonable explanations for the experiments.

As driven by Moore's law, the dimension of optoelectronic devices[10] and the piezo-phototronic device are rapidly shrinking toward nanometer scale and the fundamental effect arising from the quantum mechanics becomes increasingly important.[11] Various new devices based on quantum effects, such as molecular electronic devices,[12] spin logic devices,[13] and two-dimensional devices,[14,15] emerge and greatly enhance the performances of optoelectronic devices. The coupling between the optoelectronic effect and the quantum effect has exhibited potential prospects for some significant scientific interests[16] and promising applications,[17] which would become an important research direction of next-generation piezotronic/piezo-phototronic devices. However, previous theoretical works of the piezo-phototronic effect are limited to the semiclassical model,

Received: January 18, 2016
Accepted: April 18, 2016

 © XXXX American Chemical Society 

that is, the first-order linear approximation between optical power and injected current density.[18] The quantization of energy levels and the confinement of carriers' wave functions were not considered among these theoretical works; therefore, it was not possible to study the optical transition process in the piezo-phototronic devices with the quantum structure.

In this paper, a fundamental theoretical framework of the piezo-phototronic effect in the quantum well structure is presented with the combination of perturbation theory in quantum mechanics[19] and piezo-phototronic effect. With this methodology, we utilize the self-consistent numerical model to analyze the piezo-phototronic effect in single InGaN/GaN quantum well (SQW) and dual InGaN/GaN quantum wells (DQWs) and provide many important understandings, including the band structure, electron/hole wave function, wave function overlap, and optical transition intensity. Furthermore, accompanied by numerical calculations, photoluminescence (PL) measurements in a SQW and DQWs are conducted to effectively prove the validity and universality of our model. This theoretical work establishes the physical model for understanding the piezo-phototronic effect in the view of quantum effects and provides guidance for future device design.

As shown in Figure 1a, the framework of the piezo-phototronic effect at the nanoscale can be summarized as the coupling among the theory of semiconductors, piezoelectricity, photoexcitation, and quantum effect. From the perspective of perturbation theory, the piezo-phototronic effect on the optical transition process in the QWs can be described by four critical processes: (*i*) piezoelectric field that results from the external/internal strain; (*ii*) opposite shift of the wave function of electrons and holes under a polar field; (*iii*) redistribution of free carriers and spatial change of the energy band by the electrostatic potential; and (*iv*) optical interband transition. Their governing equations are listed below.

**(1) Constitutive Equation of Piezoelectricity.**[20] For the general theory of piezoelectricity and elasticity, the relation between strain/stress, piezoelectric polarization, and electric field can be written as

$$\begin{cases} \sigma_p = c_{pq}\varepsilon_q - e_{kp}E_k \\ D_i = e_{iq}\varepsilon_q + \kappa_{ik}E_k \end{cases} \tag{1}$$

where $\sigma_p$ is the stress tensor, $\varepsilon_q$ the strain, $E_k$ the electric field, and $D_i$ the electric displacement. The coefficients $c_{pq}$, $e_{kp}$, and $\kappa_{ik}$ are the linear elastic constant, piezoelectric coefficient, and dielectric constant, respectively.

**(2) Schrödinger Equation.** The Schrödinger equation is introduced to solve the wave function of electrons and holes in the quantum structures:

$$-\frac{\hbar^2}{2m_e^*}\nabla^2\psi_n + V = E_n\psi_n \tag{2}$$

where $\hbar$ represents the reduced Planck constant, $m_e^*$ electron effective mass, $V$ the potential function, $\psi_n$ the $n$th state wave function, with its associated $n$th state energy level $E_n$.

**(3) Poisson Equation.** The Poisson equation relates the electrostatic potential with spatial charge distribution and it is written as

$$\kappa\nabla^2\varphi = -\rho + \nabla \boldsymbol{P}_{\text{tot}} \tag{3}$$

where $\varphi$ is the potential distribution and $\rho$ is the net charge which is a nonlinear function of the potential:

$$\rho(\varphi) = [p(\varphi) + n(\varphi) + N_D^+ - N_A^-] \tag{4}$$

$p$ and $n$ denote the mobile carrier density of holes and electrons, $N_D^+$ and $N_A^-$ are totally ionized donor and acceptor densities. $\boldsymbol{P}_{\text{tot}}$ denotes the total polarization vector that is composed of spontaneous polarization $\boldsymbol{P}_{\text{sp}}$ and strain-induced piezoelectric polarization $\boldsymbol{P}_{\text{pe}}$:

$$\boldsymbol{P}_{\text{tot}} = \boldsymbol{P}_{\text{sp}} + \boldsymbol{P}_{\text{pe}} \tag{5}$$

**(4) Fermi's Golden Rule.** Based on the perturbation theory, the general formalism of optical interband transition can be represented by Fermi's golden rule, and it is expressed as

$$R = \frac{2\pi}{\hbar}\sum_{n\neq m}|\langle\psi_n|\boldsymbol{H}_+|\psi_m\rangle|^2\delta(E_m - E_n + \hbar\omega) + \frac{2\pi}{\hbar}\sum_{n\neq m}|\langle\psi_n|\boldsymbol{H}_-|\psi_m\rangle|^2\delta(E_m - E_n - \hbar\omega) \tag{6}$$

According to the perturbation theory, the Hamiltonian for quantum mechanical system is $\boldsymbol{H} = \boldsymbol{H}_0 + \boldsymbol{H}_+e^{-i\omega t} + \boldsymbol{H}_-e^{-i\omega t}$, where $\boldsymbol{H}_0$ denotes the initial Hamiltonian and a time-dependent perturbation is described by $\{\boldsymbol{H}_+e^{-i\omega t} + \boldsymbol{H}_-e^{-i\omega t}\}$. In eq 6, the transition rate between the initial state $\psi_m$ with an energy level $E_m$ to the final state $\psi_n$ with an energy level $E_n$ is denoted by $R$.

To analyze the piezo-phototronic effect in the QWs, as the first step, the formula of piezoelectric polarization and built-in electric field produced by external/internal strain should be derived. In our work, wurtzite materials grown in the polar [0001] direction are considered. For the $C_{6v}$ symmetry of the wurtzite structure, the coefficients $c_{pq}$, $e_{kp}$, and $\kappa_{ik}$ in eq 1 can be written as[21]

$$c_{pq} = \begin{bmatrix} c_{11} & c_{12} & c_{13} & 0 & 0 & 0 \\ c_{12} & c_{11} & c_{13} & 0 & 0 & 0 \\ c_{13} & c_{13} & c_{33} & 0 & 0 & 0 \\ 0 & 0 & 0 & c_{44} & 0 & 0 \\ 0 & 0 & 0 & 0 & c_{44} & 0 \\ 0 & 0 & 0 & 0 & 0 & \frac{(c_{11} - c_{12})}{2} \end{bmatrix} \tag{7a}$$

$$e_{kp} = \begin{bmatrix} 0 & 0 & 0 & 0 & e_{15} & 0 \\ 0 & 0 & 0 & e_{15} & 0 & 0 \\ e_{31} & e_{31} & e_{33} & 0 & 0 & 0 \end{bmatrix} \tag{7b}$$

$$\kappa_{ik} = \begin{bmatrix} \kappa_{11} & 0 & 0 \\ 0 & \kappa_{11} & 0 \\ 0 & 0 & \kappa_{33} \end{bmatrix} \tag{7c}$$

For ease of labeling, the coordinate system $x$–$y$ axis is parallel to the growth surface of the QW and the $z$ axis is along the polar direction [0001]. In many cases, the external strain is applied along the $c$ axis,[22] then $\sigma_{xx,v}$ and $\sigma_{zz,v}$ can be obtained as follows:

$$\sigma_{xx,v} = (C_{11,v} + C_{12,v})\varepsilon_{xx,v} + C_{13,v}\varepsilon_{zz,v} \tag{8a}$$

$$\sigma_{zz,v} = 2C_{13,v}\varepsilon_{xx,v} + C_{33,v}\varepsilon_{zz,v} + P \tag{8b}$$



DOI: 10.1021/acsnano.6b00417
ACS Nano XXXX, XXX, XXX−XXX

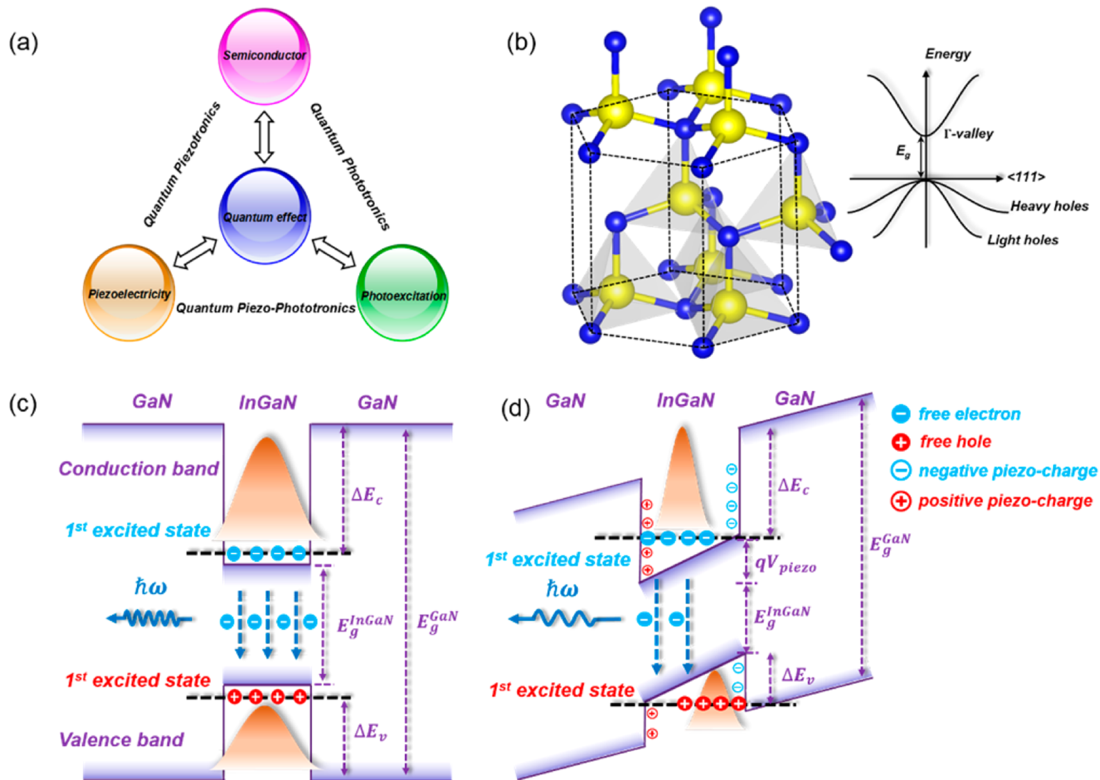


**Figure 1. Schematic diagram of the mechanism for a piezo-phototronic effect in the quantum well. (a) Multifield coupling effect among the theory of semiconductors, piezoelectricity, photoexcitation, and quantum effects. (b) Schematic of the typical atomic structure of the wurtzite unit cell and corresponding band structure (blue and yellow spheres correspond to the anion and cation atoms, respectively). Schematic potential profile and electron/hole wave function distribution (c) without and (d) with piezoelectric polarization induced by external stress along the *c* axis.**

where the index $\sigma_{xx,v}$ indices are "w" for the well and "b" for the barrier. $P$ denotes the pressure caused by external strain. Due to the free expansion along the $z$ axis,[23] the condition $\sigma_{zz,v} = 0$ leads to the following relationship between $\varepsilon_{zz,v}$ and $\varepsilon_{xx,v}$:

$$\varepsilon_{zz,v} = -\frac{2C_{13,v}}{C_{33,v}}\varepsilon_{xx,v} - \frac{P}{C_{33,v}} \tag{9a}$$

and

$$\varepsilon_{xx,v} = \frac{a_{SL} - a_v}{a_v} \tag{9b}$$

where $a_{SL}$ is the in-plane lattice constant of the barrier for $v$ = w and the well for $v$ = b. Finally, the electric field $E_{z,v}$ in the well and barrier layers can be derived according to the condition of potential continuity at the interface:[24]

$$E_{z,v} = E_{z,w}^{int} + PE_{z,w}^{ext} \tag{10a}$$

where

$$E_{z,w}^{int} = \left\{L_b\left[P_{sp,b} + 2\left(e_{31,b} - \frac{C_{13,b}}{C_{33,b}}e_{33,b}\right)\varepsilon_{xx,b} - P_{sp,w} - 2\left(e_{31,w} - \frac{C_{13,w}}{C_{33,w}}e_{33,w}\right)\varepsilon_{xx,w}\right]\right\}/(L_b\kappa_w + L_w\kappa_b) \tag{10b}$$

$$E_{z,w}^{ext} = \frac{L_b\left(\frac{e_{33,w}}{C_{33,w}} - \frac{e_{33,b}}{C_{33,b}}\right)}{L_b\kappa_w + L_w\kappa_b} \tag{10c}$$

In eq 10a, the symbols $E_{z,w}^{int}$ and $E_{z,w}^{ext}$ represent the electric field induced by the lattice mismatch between the interfaces and external strain, respectively. Widths of the wells and barriers are indicated by $L_w$ and $L_b$, respectively. The electric field in the barrier can be obtained just by changing indices w to b from eq 10a to eq 10c.

Substituting eqs 10a–10c into eq 2 as the second step, the wave function of electrons and related energy level can be solved from the Schrödinger–Poisson equations. Specifically, the potential function $V$ in eq 2 can be derived as $V = -q\varphi + \Delta E_c$, where $\Delta E_c$ represents the band offset and $\varphi$ denotes the electrostatic potential calculated by the Poisson equation. This method can also be used to solve the wave function and corresponding energy level for holes by changing the $m_e^*$ and $\Delta E_c$ to the hole effective mass $m_h^*$ and band offset $\Delta E_v$.

Finally, with the distribution of the wave functions of the electrons and holes, the optical transition intensity $W$, which is proportional to radiative recombination rate $R$, can be derived from eq 6. Considering the confinement along the [0001] direction and properties of Bloch functions in the QWs,[25] eq 6, as the general formula of Fermi's golden rule, can be further developed into the explicit formula with parabolic dispersion approximation near the extremum of the energy band[26] and expansion by a Gaussian line shape function:[27]



DOI: 10.1021/acsnano.6b00417
ACS Nano XXXX, XXX, XXX−XXX

$$W = \frac{2C_0}{L} |\Gamma_{\mathrm{cv}}^{mn}|^2 \langle |\boldsymbol{P}_{\mathrm{cv}} \cdot \boldsymbol{n}|^2 \rangle \int \frac{\mathrm{d}^2 k}{(2\pi)^2} \frac{f_{\mathrm{c}}^m (k_{\parallel})[1 - f_{\mathrm{v}}^n (k_{\parallel})](\zeta/2\pi)}{(E_{\mathrm{c}}^m - E_{\mathrm{v}}^n - \hbar\omega)^2 + (\zeta/2)^2} \tag{11a}$$

In eq 11a, $W$ describes the optical transition intensity related to $m$th state in the conduction band and $n$th state in the valence band. Here, the script c and v represent the conduction and valence bands, respectively; $\langle |\boldsymbol{P}_{\mathrm{cv}} \cdot \boldsymbol{n}|^2 \rangle$ is the average value of the squared momentum matrix element; $f_{\mathrm{c}}$ and $f_{\mathrm{v}}$ represent the Fermi–Dirac distribution function in the conduction and valence bands, respectively; $L$ is the QW width; $k_{\parallel}$ is the wavevector perpendicular to the $c$ axis; $\zeta$ is the line width due to the scattering, and $\Gamma_{\mathrm{cv}}^{mn}$ is the electron–hole wave function overlap integral:

$$\Gamma_{\mathrm{cv}}^{mn} = \int \mathrm{d}z (\psi_{\mathrm{c}}^m (z))^* \psi_{\mathrm{v}}^n (z) \tag{11b}$$

and the coefficient

$$C_0 = \frac{q^2 \eta \omega}{\pi \kappa_0 \hbar c_1^3 m_0^2} \tag{11c}$$

where $\eta$ is the refractive index in the QWs, $m_0$ represents the electron rest mass, and $c_1$ and $\kappa_0$ are the velocity of light and permittivity in the free space, respectively.

In eq 11a, we notice that the integral term over $k_{\parallel}$ related to the quantum-confined energy level and squared momentum matrix element $|\boldsymbol{P}_{\mathrm{cv}} \cdot \boldsymbol{n}|^2$, which represents the product between momentum of carriers and photon, is determined by the physical parameters of the QWs and polar direction of injected light beam. Generally, eqs 11a–11c describe a linear relationship between the optical transition intensity $W$ and overlap of electron–hole wave function overlap $\Gamma_{\mathrm{cv}}^{mn}$.

To provide qualitative understanding how the piezo-phototronic effect tunes the optical transition process, the schematic of energy band diagrams is shown in Figure 1c,d. When the QWs are released from the strain (Figure 1c), the wave functions of electrons and holes are symmetrically distributed along the $z$ axis, and the corresponding shadow area, which represents the wave function overlap integral of electron–hole pairs in the real space, reaches the maximum when the band remains flat. Under the tensile or compressive straining condition (Figure 1d), the positive/negative piezo-charges accumulate at the left/right side and they induce a linear tilt of the band in the QWs. Then the wave functions of electrons and holes are separated in opposite directions in the tilt band, which reduces the wave function overlap to a lower radiative recombination rate.

A self-consistent numerical calculation is performed using the finite difference method within the effective mass approximation.[28] Equations 8–10 give the distribution of external strain qualitatively; however, the strain distribution was much more complex than the uniaxial/biaxial strain model in practice. In our work, the strain distribution of GaN/InGaN nanopillars was simulated by a finite element method (discussed in the Supporting Information). We focus on the energies of the interband transition under the normal low-power excitation; thus, only the lowest sub-band states and energy levels for electrons and holes are taken into account during the calculation. The calculations are conducted to present the optical transition in arbitrary GaN/InGaN SQWs and DQWs. In this case, to ensure accuracy in comparison between experiments and calculations, these GaN/InGaN QWs were etched to nanopillars to release the internal strain induced by the lattice mismatch and enhance the piezo-phototronic effect. The detailed calculation parameters for wurtzite GaN and InN are listed in Table 1, and for the corresponding $In_xGa_{1-x}N$ ternary alloys, the parameters are calculated with the linear interpolation of Vegard's law.[29]

**Table 1. Value List of Physical Parameters for Wurtzite GaN and InN Calculated in This Work**

| parameters | GaN | InN | refs |
|---|---|---|---|
| lattice constant (nm) | | | |
| $a$ | 0.319 | 0.355 | 30 |
| $c$ | 0.519 | 0.570 | 30 |
| energy parameters at 300 K | | | |
| $E_g$ (eV) | 3.437 | 0.641 | 30 |
| $m_e/m_0$ | 0.20 | 0.07 | 30 |
| $m_{hh}/m_0$ | 1.56 | 1.27 | 31 |
| $\varepsilon/\varepsilon_0$ | 10.40 | 15.30 | 32 |
| elastic stiffness constants (GPa) | | | |
| $C_{11}$ | 390 | 223 | 30 |
| $C_{12}$ | 145 | 115 | 30 |
| $C_{13}$ | 106 | 92 | 30 |
| $C_{33}$ | 398 | 224 | 30 |
| piezoelectric constant ($C/m^2$) | | | |
| $e_{31}$ | −0.49 | −0.57 | 33 |
| $e_{33}$ | 0.73 | 0.97 | 33 |
| $P_{sp}$ | −0.029 | −0.032 | 33 |

To obtain a self-consistent solution of basic equations, an iteration between the Schrödinger–Poisson equation system is conducted by a three-point finite difference method.[34] During the self-consistent calculation, the conduction/valence band offset ratio, which describes the details of conduction/valence band alignment, takes the common value of 7:3.[35,36] A grid spacing as small as $1 \times 10^{-10}$ m along the $z$ axis and the convergent criteria for the electrostatic potential is set to be 0.1% to ensure the iteration convergence and stability of our calculation.

## RESULTS AND DISCUSSION

For explicit analysis of the piezo-phototronic effect in the QWs, the self-consistent calculation based on the SQW of the GaN/$In_{0.25}Ga_{0.75}N$ nanopillar structure was conducted, and the results are demonstrated in Figure 2a–c. In Figure 2a, with an external strain applied on the SQW, piezo-charges are induced at two ends of GaN barrier and interfaces between GaN and $In_{0.25}Ga_{0.75}N$. For the profile of piezo-charges in our model, it should be noted that, unlike the condition of lattice-mismatched piezoelectric polarization whose strain direction is opposite of each other at the GaN/$In_xGa_{1-x}N$ interfaces, the external strain dominates invariably across the well and barriers, which results in partial compensation at the interfaces. For details in the diagram, the piezo-charge (marked by a black line) is up to ±0.01 $C/m^2$ at two ends with a compressive strain of −0.4%. The ±0.01 and ±0.012 $C/m^2$ (marked by blue and yellow dotted lines) accumulate at the interfaces of GaN and $In_{0.25}Ga_{0.75}N$ sides, respectively, with the remnant piezo-charges of 0.002 $C/m^2$ at the interfaces.

With the effect of a piezoelectric polarization-induced electric field, the energy band diagram and corresponding overlap of electron and hole wave functions are shown in Figure 2b,c,



DOI: 10.1021/acsnano.6b00417
ACS Nano XXXX, XXX, XXX–XXX

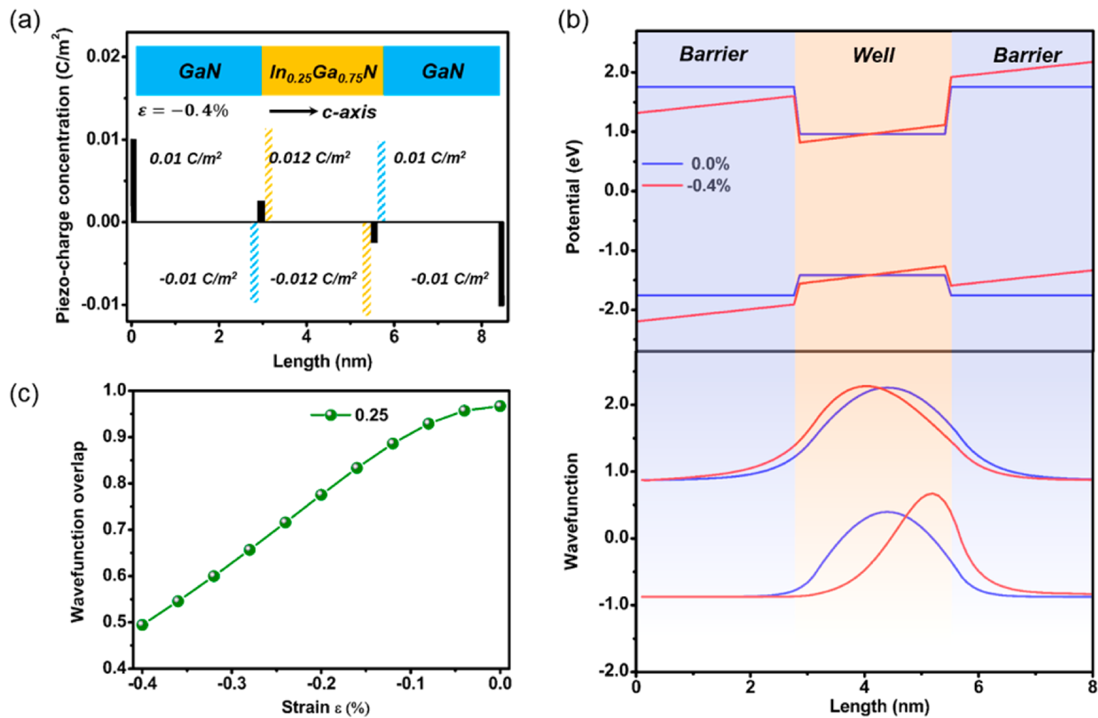


**Figure 2.** Schematic diagram of the piezo-phototronic effect in a GaN/$In_{0.25}Ga_{0.75}N$ single quantum well. (a) Profile of piezo-charges at the interface with external compressive strain of 0.4%. The black solid lines correspond to the net piezo-charges, and the piezo-charges produced by barriers (green) and wells (yellow) are represented by dotted lines. (b) Self-consistent energy band and wave function distribution in an $In_{0.25}Ga_{0.75}N$/GaN single quantum well from top to bottom. (c) Electron−hole wave function overlap as a function of compressive strain from 0 to 0.4%.

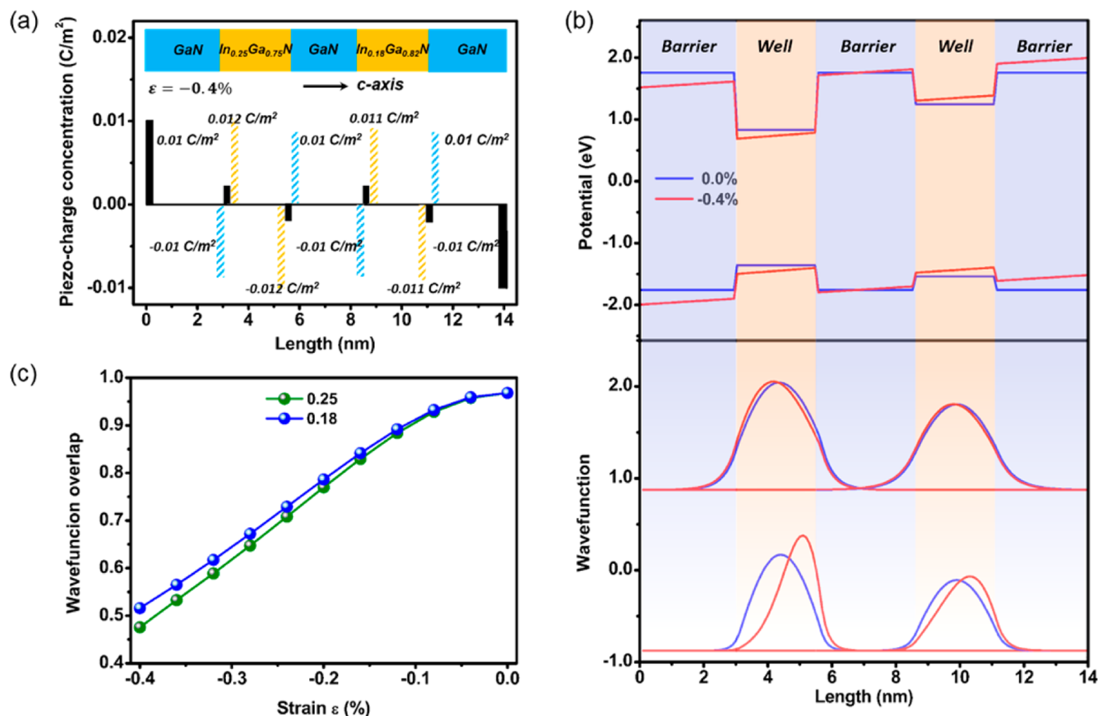


**Figure 3.** Schematic diagram of piezo-phototronic effect on GaN/$In_{0.25}Ga_{0.75}N$ ($In_{0.18}Ga_{0.82}N$) dual quantum well. (a) Profile of piezo-charges at the interface with external compressive strain of 0.4%. The black solid lines correspond to the net piezo-charges, and the piezo-charges produced by barriers (green) and wells (yellow) are represented by dotted lines. (b) Self-consistent energy band and wave function distribution on the GaN/$In_{0.25}Ga_{0.75}N$ ($In_{0.18}Ga_{0.82}N$) dual quantum well from top to bottom. (c) Electron−hole wave function overlap as a function of compressive strain from 0 to 0.4%.

respectively. As can be easily seen, in the release condition, the conduction and valence bands of the SQW are perceived to be nearly flat for the GaN/$In_{0.25}Ga_{0.75}N$ nanopillar structure, although with weak spontaneous polarization, and the wave



DOI: 10.1021/acsnano.6b00417
ACS Nano XXXX, XXX, XXX−XXX

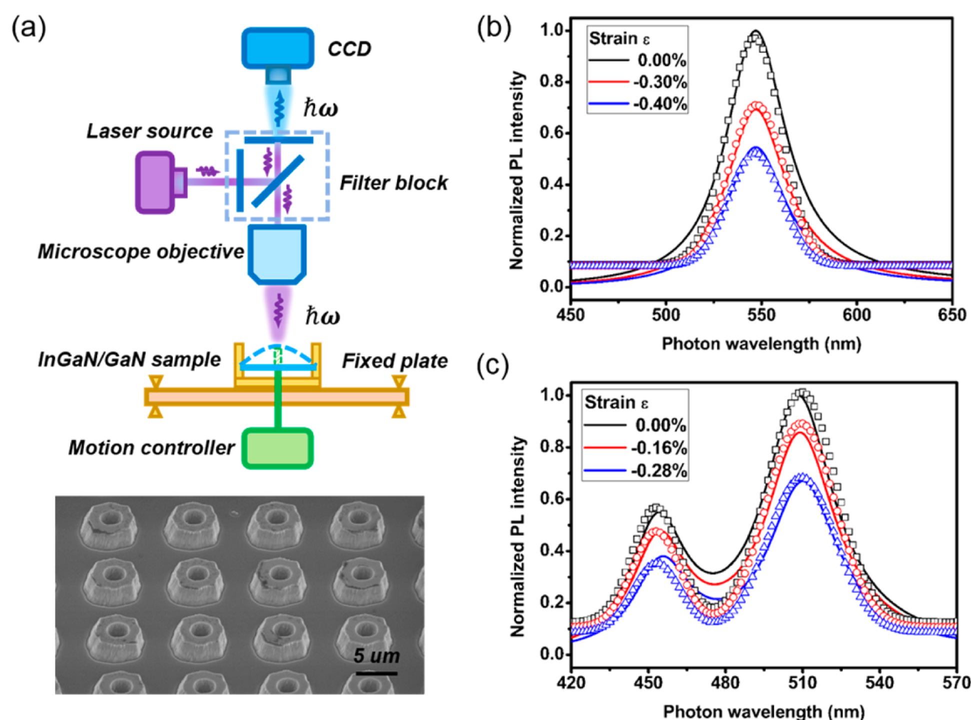


**Figure 4. Comparison of the measured PL spectrum with the self-consistent numerical calculations. (a) Schematic diagram of the PL experiment inset with a SEM image of the GaN/InGaN sample. (b,c) Numerical PL spectrum data based on our self-consistent model (solid lines) and measured PL spectrum in the experiment (squares, circles, and triangles) under different compressive strains.**

functions of the electron/hole are symmetrical with respect to the SQW *c* axis. Under this condition, in Figure 2c, we notice that the wave functions of the electrons and holes are effectively overlapped, and the overlap integral of normalized wave functions is close to 1, which results in a high optical transition and emission efficiency. Under the compressive strain of −0.4%, the electric field of 0.6 MV/cm along the *c* axis is induced by piezo-charges and the band bending occurs with unsymmetrical distribution of the wave functions of the electrons/holes. As shown in Figure 2c, with compressive strains from 0.0 to −0.4% in the SQW, the piezoelectric electric field increases and linearly decreases the overlap integral from 1 to 0.5, and it can be attributed to the enhanced separation of the wave functions of electrons and holes in the opposite direction.

Besides the SQW structure, the multiquantum wells have been widely used in solid lighting, displays, and visible light communication.[37] To verify the universality of our model, an asymmetric DQW of the GaN/$In_{0.25}Ga_{0.75}N$ ($In_{0.18}Ga_{0.82}N$) nanopillar structure is also calculated, and corresponding numerical results are given in Figure 3a−c. Figure 3a shows the piezo-charge distributions in the complex DQWs of GaN/$In_{0.25}Ga_{0.75}N$ ($In_{0.18}Ga_{0.82}N$). In Figure 3b, the conduction band and valence band are both tilted by the strain-induced piezoelectric field. Different from the SQW, a pair of ground states for electrons and holes exist in the DQWs of $In_{0.25}Ga_{0.75}N$ and $In_{0.18}Ga_{0.82}N$. It can also be noticed that the variation of hole wave functions with respect to the piezoelectric electric field is more sensitive than electron wave functions and can be attributed to the effective mass of holes being larger than that of electrons.[38] In Figure 3c, the overlap integral for the wave functions of the electrons and holes in the DQWs gradually decreases with compressive strain, and the variation value of the $In_{0.25}Ga_{0.75}N$ well is slightly higher than that of the SQW (Figure 2c). The slight difference between $In_{0.25}Ga_{0.75}N$ and $In_{0.18}Ga_{0.82}N$ results from various compounds in the well, and we will talk about it in detail in the following section.

For comparison with the numerical results, PL measurements under various compressive strains are employed, and the sketch of the experiment is shown in Figure 4a. The sample of the GaN/InGaN nanopillar is fixed by a jig with a jackscrew pinning at the back of the plate. Manipulated by the motion controller, the jackscrew can be screwed forward perpendicular to the GaN/InGaN sample, and compressive strain is induced along the *c* axis direction due to the in-plane expansion along the GaN/InGaN sample. An ultraviolet laser with an excitation wavelength of 325 nm is illuminated from the top, and a charge-coupled device (CCD) was used to detect light intensity. The GaN/InGaN QW nanopillar array on a *c* plane sapphire substrate was obtained with a basic lithography etching technique, and a relevant scanning electron microscope (SEM) image is displayed in the inset of Figure 4a. Comparison between the PL spectra and results of self-consistent calculations are shown in Figure 4b,c. For the case of the SQW (Figure 4b), we found an excellent agreement between the theoretical spectra and measured PL spectra. With the *c*-axial strains from 0.0 to −0.4%, the maximum of normalized PL intensity decreases from 1 to almost 0.5 due to the spatial separation of the wave function of the electrons and holes. For the DQW sample (Figure 4c), the theoretical spectra and the measured PL spectra are fitted quite well near 425 and 510 nm, which corresponds to the emission peak of $In_{0.18}Ga_{0.82}N$ and $In_{0.25}Ga_{0.75}N$, respectively. Some tiny deviations between theoretical and measured PL spectra appear around 470−490 nm, and the reason can be attributed to the overestimation of the phonon effect to enhance the coupling of quantum states when we take the perturbation theory to describe the quasi-



DOI: 10.1021/acsnano.6b00417
*ACS Nano* XXXX, XXX, XXX−XXX

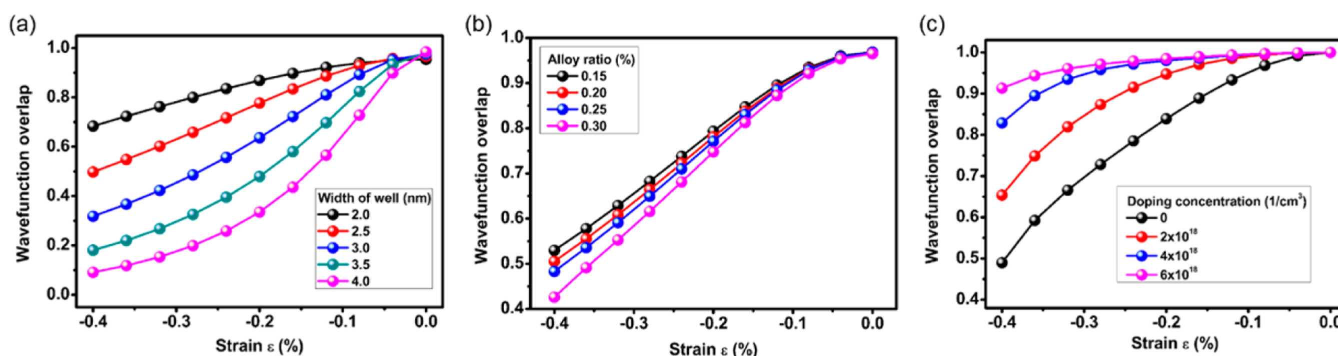


**Figure 5. Electron−hole wave function overlap dependency of (a) various widths of well, (b) indium content, and (c) donor concentrations in the single GaN/$In_{0.25}Ga_{0.75}N$ QW.**

steady-state emission.[39] Furthermore, the statistical bias that results from the rough meshing near the band tails is also a possible reason.

Next, we then controlled the parameters related to the device structure such as quantum well size, content, and dopant and studied the optimization of the quantum piezo-phototronic effect based on our model.

As a key parameter to modulate the quantum-confined energy level in the QWs, the effect of quantum well width was studied. As shown in Figure 5a, when the width of well varies from 2.0 to 4.0 nm, and the variation of wave functions with respect to strain $\Gamma_{cv}^{mn}/\varepsilon$ was quite enhanced and was caused by the greater magnitude of piezopotential, which is proportional to the well width. During the design and fabrication of light-emitting diodes, a certain wavelength of lighting diode is mainly determined by the indium content in the well. Figure 5b shows the wave function overlap curves under different strain conditions with various indium contents. When the indium content increases from 0.15 to 0.30, $\Gamma_{cv}^{mn}/\varepsilon$ tends to slightly increase. When the indium content increases, based on the linear interpolation of Vegard's law, the larger piezoelectric coefficient of $In_xGa_{1-x}N$ is obtained, which induces more remnant piezo-charges at the interfaces. This conclusion is consistent with the former results obtained in Figure 3c. The green gap is a significant issue in group III nitride optoelectronic devices, and thus we should pay more attention to the higher strain responsivity in the high indium content QWs.

Besides the quantum well width and magnitude of the compound, the effect of the carrier screening effect is also an essential factor for the piezo-phototronic performance especially for carrier density at $n = 2 \times 10^{19}$ $cm^{-3}$ and higher.[40] In Figure 5c, it is noticed that when the strain increases from 0 to −0.4%, the wave function overlap decreases from 1 to 0.5 without doping and from 1 to 0.9 under the doping concentration of $6 \times 10^{18}$ $cm^{-3}$. It suggests that the influence of the quantum piezo-phototronic effect will be greatly diminished with high doping, and a relatively lower free carrier concentration is desired for the optimization of quantum piezo-phototronic effect in the QWs.

## CONCLUSION

In summary, we have presented the theoretical framework for a piezo-phototronic effect from the point of perturbation theory in quantum mechanics. The general governing equations are introduced for illustrating the physical mechanism of piezo-phototronics in a quantum structure, and the calculation results provide a comprehensive understanding of the piezo-phototronic effect on the optical interband process. The good agreements between the PL experiments and self-consistent calculation in the SQW and DQWs of GaN/InGaN support a quantitative evaluation and verification of numerical results expected from the theory. Using this methodology, we also studied the effect of structure parameters on the optical transition process, and strategy was provided for optimization of piezo-phototronic devices. Our work not only presents the physical insights into piezo-phototronic effect in the quantum structure but also provides the theoretical support to guide the future design of piezo-phototronic devices.

## EXPERIMENTAL METHODS

The InGaN/GaN SQW and DQW structures were grown on [0001]-oriented sapphire substrates by metal−organic chemical vapor deposition. The gallium, indium, and nitrogen sources were trimethylgallium, triethylgallium, trimethylindium, and ammonia. We used silane and biscyclopentadienyl magnesium as n-type and p-type dopants, respectively. The SQW and DQW nanopillar arrays were obtained with a basic lithography etching technique. A 200 nm thick silica film was first deposited, followed by a spin-coated 2 $\mu$m thick photoresist (ARU 4030). The low-damage dry etching of GaN-based thin film by inductively coupled plasma was conducted for 8 min, and silica residue was removed by diluted hydrochloric acid for 5 min. PL measurements of GaN/InGaN SQW and MQW samples were measured at room temperature by LabRam HR Evolution with a beam spot size of 1 $\mu$m.

## ASSOCIATED CONTENT

### Supporting Information

The Supporting Information is available free of charge on the ACS Publications website at DOI: 10.1021/acsnano.6b00417.

Experimental details and Figure S1 (PDF)

## AUTHOR INFORMATION

### Corresponding Authors

*E-mail: huweiguo@binn.cas.cn.
*E-mail: hchen@iphy.ac.cn.
*E-mail: zlwang@gatech.edu.

### Author Contributions

⊥X.H. and C.D. contributed equally.

### Notes

The authors declare no competing financial interest.



DOI: 10.1021/acsnano.6b00417
ACS Nano XXXX, XXX, XXX−XXX

## ACKNOWLEDGMENTS

The authors thank the "Thousands Talents" program for pioneer researcher and his innovation team, One Hundred Person Project of the Chinese Academy of Sciences, and the National Natural Science Foundation of China (Grant Nos. 51432005 and 61574018) for the support.

## REFERENCES

(1) Pan, Z. W.; Dai, Z. R.; Wang, Z. L. Nanobelts of Semiconducting Oxides. *Science* **2001**, *291*, 1947−1949.
(2) Wang, Z. L.; Song, J. Piezoelectric Nanogenerators Based on Zinc Oxide Nanowire Arrays. *Science* **2006**, *312*, 242−246.
(3) Pan, C.; Dong, L.; Zhu, G.; Niu, S.; Yu, R.; Yang, Q.; Liu, Y.; Wang, Z. L. High-Resolution Electroluminescent Imaging of Pressure Distribution Using a Piezoelectric Nanowire LED Array. *Nat. Photonics* **2013**, *7*, 752−758.
(4) Yang, Q.; Wang, W.; Xu, S.; Wang, Z. L. Enhancing Light Emission of ZnO Microwire-Based Diodes by Piezo-Phototronic Effect. *Nano Lett.* **2011**, *11*, 4012−4017.
(5) Li, X.; Chen, M.; Yu, R.; Zhang, T.; Song, D.; Liang, R.; Zhang, Q.; Cheng, S.; Dong, L.; Pan, A.; et al. Enhancing Light Emission of ZnO-Nanofilm/Si-Micropillar Heterostructure Arrays by Piezo-Phototronic Effect. *Adv. Mater.* **2015**, *27*, 4447−4453.
(6) Pan, C.; Guo, W.; Dong, L.; Zhu, G.; Wang, Z. L. Optical Fiber-Based Core-Shell Coaxially Structured Hybrid Cells for Self-Powered Nanosystems. *Adv. Mater.* **2012**, *24*, 3356−3361.
(7) Wang, X.; Zhang, H.; Yu, R.; Dong, L.; Peng, D.; Zhang, A.; Zhang, Y.; Liu, H.; Pan, C.; Wang, Z. L. Dynamic Pressure Mapping of Personalized Handwriting by a Flexible Sensor Matrix Based on the Mechanoluminescence Process. *Adv. Mater.* **2015**, *27*, 2324−2331.
(8) Zhang, Y.; Wang, Z. L. Theory of Piezo-Phototronics for Light-Emitting Diodes. *Adv. Mater.* **2012**, *24*, 4712−4718.
(9) Liu, Y.; Niu, S.; Yang, Q.; Klein, B. D.; Zhou, Y. S.; Wang, Z. L. Theoretical Study of Piezo-Phototronic Nano-LEDs. *Adv. Mater.* **2014**, *26*, 7209−7216.
(10) Schaller, R. R. Moore's Law: Past. *IEEE Spectrum* **1997**, *34*, 52−59.
(11) Pan, C.; Chen, M.; Yu, R.; Yang, Q.; Hu, Y.; Zhang, Y.; Wang, Z. L. Progress in Piezo-Phototronic-Effect-Enhanced Light-Emitting Diodes and Pressure Imaging. *Adv. Mater.* **2016**, *28*, 1535−1552.
(12) Song, H.; Reed, M. A.; Lee, T. Single Molecule Electronic Devices. *Adv. Mater.* **2011**, *23*, 1583−1608.
(13) Behin-Aein, B.; Datta, D.; Salahuddin, S.; Datta, S. *Nat. Nanotechnol.* **2010**, *5*, 266−270.
(14) Fiori, G.; Bonaccorso, F.; Iannaccone, G.; Palacios, T.; Neumaier, D.; Seabaugh, A.; Banerjee, S. K.; Colombo, L. Electronics Based on Two-Dimensional Materials. *Nat. Nanotechnol.* **2014**, *9*, 768−779.
(15) Huang, X.; Liu, W.; Zhang, A.; Zhang, Y.; Wang, Z. Ballistic Transport in Single-Layer $MoS_2$ Piezotronic Transistors. *Nano Res.* **2016**, *9*, 282−290.
(16) Peng, M.; Zhang, Y.; Liu, Y.; Song, M.; Zhai, J.; Wang, Z. L. Magnetic-Mechanical-Electrical-Optical Coupling Effects in GaN-Based LED/Rare-Earth Terfenol-D Structures. *Adv. Mater.* **2014**, *26*, 6767−6772.
(17) Du, C.; Jiang, C.; Zuo, P.; Huang, X.; Pu, X.; Zhao, Z.; Zhou, Y.; Li, L.; Chen, H.; Hu, W.; et al. Piezo-Phototronic Effect Controlled Dual-Channel Visible light Communication (PVLC) Using InGaN/GaN Multiquantum Well Nanopillars. *Small* **2015**, *11*, 6071−6077.
(18) Faist, J.; Capasso, F.; Sirtori, C.; Sivco, D. L.; Hutchinson, A. L.; Cho, A. Y. Laser Action by Tuning the Oscillator Strength. *Nature* **1997**, *387*, 777−782.
(19) Chuang, S. L. Optical Gain of Strained Wurtzite GaN Quantum-Well Lasers. *IEEE J. Quantum Electron.* **1996**, *32*, 1791−1800.
(20) Gao, Y.; Wang, Z. L. Electrostatic Potential in a Bent Piezoelectric Nanowire. The Fundamental Theory of Nanogenerator and Nanopiezotronics. *Nano Lett.* **2007**, *7*, 2499−2505.
(21) Chuang, S.; Chang, C. k· p Method for Strained Wurtzite Semiconductors. *Phys. Rev. B: Condens. Matter Mater. Phys.* **1996**, *54*, 2491−2504.
(22) Zhao, Z.; Pu, X.; Han, C.; Du, C.; Li, L.; Jiang, C.; Hu, W.; Wang, Z. L. Piezotronic Effect in Polarity-Controlled GaN Nanowires. *ACS Nano* **2015**, *9*, 8578−8583.
(23) Christmas, U. M. E.; Andreev, A. D.; Faux, D. A. Calculation of Electric Field and Optical Transitions in InGaN/GaN Quantum Wells. *J. Appl. Phys.* **2005**, *98*, 073522.
(24) Fiorentini, V.; Bernardini, F.; Della Sala, F.; Di Carlo, A.; Lugli, P. Effects of Macroscopic Polarization in III-V Nitride Multiple Quantum Wells. *Phys. Rev. B: Condens. Matter Mater. Phys.* **1999**, *60*, 8849−8858.
(25) Chuang, S.; Chang, C. A Band-Structure Model of Strained Quantum-Well Wurtzite Semiconductors. *Semicond. Sci. Technol.* **1997**, *12*, 252−263.
(26) Smith, D. L.; Mailhiot, C. k·p Theory of Semiconductor Superlattice Electronic Structure. I. Formal results. *Phys. Rev. B: Condens. Matter Mater. Phys.* **1986**, *33*, 8345−8359.
(27) Xiao, D.; Kim, K. W.; Zavada, J. M. Envelope-Function Analysis of Wurtzite InGaN/GaN Quantum Well Light Emitting Diodes. *J. Appl. Phys.* **2004**, *96*, 723−728.
(28) Miller, D.; Chemla, D.; Damen, T.; Gossard, A.; Wiegmann, W.; Wood, T.; Burrus, C. Band-edge Electroabsorption in Quantum Well Structures: the Quantum-Confined Stark Effect. *Phys. Rev. Lett.* **1984**, *53*, 2173−2176.
(29) Denton, A. R.; Ashcroft, N. W. Vegard's Law. *Phys. Rev. A: At., Mol., Opt. Phys.* **1991**, *43*, 3161−3164.
(30) Vurgaftman, I.; Meyer, J. Band Parameters for Nitrogen-Containing Semiconductors. *J. Appl. Phys.* **2003**, *94*, 3675−3696.
(31) Yeo, Y.; Chong, T.; Li, M. Electronic Band Structures and Effective-Mass Parameters of Wurtzite GaN and InN. *J. Appl. Phys.* **1998**, *83*, 1429−1436.
(32) Shimada, K.; Sota, T.; Suzuki, K. First-Principles Study on Electronic and Elastic Properties of BN, AlN, and GaN. *J. Appl. Phys.* **1998**, *84*, 4951−4958.
(33) Bernardini, F.; Fiorentini, V.; Vanderbilt, D. Spontaneous Polarization and Piezoelectric Constants of III−V Nitrides. *Phys. Rev. B* **1997**, *56*, 10024−10027.
(34) Tan, I. H.; Snider, G.; Chang, L.; Hu, E. A Self-Consistent Solution of Schrödinger-Poisson Equations Using a Nonuniform Mesh. *J. Appl. Phys.* **1990**, *68*, 4071−4076.
(35) Martin, G.; Botchkarev, A.; Rockett, A.; Morkoc, H. Valence-Band Discontinuities of Wurtzite GaN, AlN, and InN Heterojunctions Measured by X-Ray Photoemission Spectroscopy. *Appl. Phys. Lett.* **1996**, *68*, 2541−2543.
(36) Domen, K.; Soejima, R.; Kuramata, A.; Tanahashi, T. Electron Overflow to the AlGaN p-Cladding Layer in InGaN/GaN/AlGaN MQW Laser Diodes. *MRS Internet J. Nitride Semicond. Res.* **1998**, *3*, 2−7.
(37) Grobe, L.; Paraskevopoulos, A.; Hilt, J.; Schulz, D.; Lassak, F.; Hartlieb, F.; Kottke, C.; Jungnickel, V.; Langer, K.-D. High-Speed Visible Light Communication Systems. *IEEE Commun. Mag.* **2013**, *51*, 60−66.
(38) McIlroy, P. W. A. Effect of an Electric Field on Electron and Hole Wave Functions in a Multiquantum Well Structure. *J. Appl. Phys.* **1986**, *59*, 3532−3536.
(39) Feldmann, J.; Peter, G.; Göbel, E.; Dawson, P.; Moore, K.; Foxon, C.; Elliott, R. Linewidth Dependence of Radiative Exciton Lifetimes in Quantum Wells. *Phys. Rev. Lett.* **1987**, *59*, 2337−2340.
(40) Zhao, H.; Arif, R.; Ee, Y.-K.; Tansu, N. Self-Consistent Analysis of Strain-Compensated InGaN−AlGaN Quantum Wells for Lasers and Light-Emitting Diodes. *IEEE J. Quantum Electron.* **2009**, *45*, 66−78.



DOI: 10.1021/acsnano.6b00417
*ACS Nano* XXXX, XXX, XXX−XXX